



Magnetic Resonance of Excited States in Semiconductors and Related Nanostructures

Pavel G. Baranov¹ · Roman A. Babunts¹ · Nikolai G. Romanov¹

Received: 30 May 2024 / Revised: 27 July 2024 / Accepted: 31 July 2024 /
Published online: 6 August 2024

© The Author(s), under exclusive licence to Springer-Verlag GmbH Austria, part of Springer Nature 2024

Abstract

Electron and nuclear spins in solids, coherently coupled to photons, provide promising resources for quantum information processing and sensing. Obtaining information about short-lived excited states is critical for realizing ultrafast all-optical spin control methods. After a brief review of early magnetic resonance studies of excited states, the following representative examples of the use of magnetic resonance spectroscopy to study excited states in wide-gap materials, semiconductors and nanostructures based on them will be considered: (1) optically detected magnetic resonance (ODMR), electron spin echo, electron-nuclear double resonance in the excited state on the example of self-trapped excitons in ionic-covalent silver halide crystals and nanocrystals, (2) ODMR and level anticrossing (LAC) spectroscopy of localized heavy-hole excitons in semiconductor quantum wells and superlattices, (3) LAC and ODMR in excited states of spin centers in diamond and silicon carbide, (4) the use of LAC and cross-relaxation for all-optical sensing with submicron spatial resolution.

1 Introduction

Following the invention of electron paramagnetic resonance (EPR) in 1944, there was a growing interest in the detailed study of excited states using magnetic resonance. Specifically, it was desirable to study excited states with the high resolution of EPR which has been successfully applied to the study of ground states. In the attempt to detect the microwave absorption directly in the excited states one is generally hampered by the fact that the number of ions that can be maintained in these excited states by optical excitation, is far too small; i.e., the combination of factors such as pumping power available, optical absorption, and lifetime of the excited state results in a number of ions in the excited state being below the

✉ Nikolai G. Romanov
nikolai.romanov@mail.ioffe.ru

¹ Ioffe Institute, St. Petersburg 194021, Russia

sensitivity of conventional EPR techniques. However, it has been realized that if the excited state in question is fluorescent, one can seek to monitor a change in the fluorescence intensity from this level when the microwave frequency coincides with its Zeeman splitting, rather than monitor the absorption of microwave power. Because optical rather than microwave photons are detected, sensitivity several orders of magnitude higher can be achieved.

The idea of double microwave-optical resonance was suggested by Brossel and Kastler [1] and the first observation of optically detected magnetic resonance (ODMR) in the excited state has been done by Brossel and Bitter [2]. It represents the magnetic resonance in the 3P_1 state of the mercury atom detected by observing the σ -polarized fluorescence. Thus, ODMR started from the study of excited states. The double resonance method allowing the investigation of excited atomic states has been extended by A. Kastler to ground states, giving birth to the optical pumping method [3] that is now widely used. The review of early works in the field of ODMR in gases that formed the basis of ODMR can be found in Ref. [4].

The first observation of ODMR in solids has been made in the excited 2E state of Cr^{3+} in Al_2O_3 crystals [5]. It is to be noted that the excited state lifetime in this case is ca. 3 ms and it was relatively easy both to create a sufficient number of centers in the excited state and to reorient the spins at EPR. Nowadays excited states with lifetime in the nanosecond range can be studied by ODMR [6, 7]. Early works on ODMR in the excited state of transition and rare earth ions in crystals are described in Ref. [8].

A special role in ODMR studies belongs to photo-excited triplet ($S=1$) states that have long lifetime (in the millisecond range) because the deexcitation into singlet ground state is spin-forbidden. The initial splitting of the $S=1$ spin levels allows ODMR measurements in zero magnetic field, which is widely investigated in biological molecules [9–12]. Excited triplet states were also studied for ions with electron configuration ns^2 (i.g. Ga^+ , Ge^{2+}) [13, 14] and self-trapped excitons in ionic crystals [15, 16], triplet excitons in semiconductors such as GaS and GaSe [17, 18] and in opto-electronic and photovoltaic materials and devices [19].

ODMR was applied to study the excited state of F-centers in alkali halide crystals. The F-center, i.e., an electron captured by an anion vacancy, is one of the simplest defects encountered in solids; moreover, it is a prototype of more complex localized electron states. Fast relaxation of the crystal lattice in the vicinity of the excited F-center leads to the formation of a relaxed excited state (RES) that emits light. The nature of this state was under debate for many years. Due to existence of spin memory in the optical pumping cycle of F-centers, EPR in both the ground and excited states could be detected by monitoring magnetic circular dichroism (MCD) in absorption [20]. Another way to study ODMR in the relaxed excited state of F-centers via photoluminescence intensity is based on the existence of a spin-dependent non-radiative deexcitation channel [21]. The studies of alkali halide crystals with different cations including isotope enriched crystals allowed to clarify the spatial extension of the RES wavefunction [22]. They led to the conclusion that the RES wavefunction of the F-center is rather a localized 2s-like state than a diffused 2p-like state, which was confirmed by calculations reported in Ref. [23].

In the present paper, we consider several characteristic examples of the use of magnetic resonance spectroscopy methods for studying short-lived excited states in ionic-covalent silver halide crystals and nanocrystals, GaAs/AlAs superlattices, spin-1 and spin-3/2 centers in diamond and silicon carbide and their use for all-optical sensing.

2 Self-Trapped Excitons in Silver Halide Crystals and Nanocrystals

2.1 ODMR in Bulk AgCl Crystals

Silver halides have unique features in solid state physics because their properties are considered to be of borderline nature between ionic and covalent bonding. In silver chloride, a self-trapped exciton (STE) is created upon ultraviolet irradiation of a crystal at low temperatures. A hole is self-trapped on Ag^+ ion in a $d_x^2-y^2$ -type orbital as the result of a Jahn–Teller distortion of the Ag coordination sphere along a cubic axis. Although this self-trapped hole (STH) is largely located at a Ag^+ ion, its wave function also contains contributions from the $3s$ and $3p$ orbitals of the neighboring Cl^- ions in the plane perpendicular to the distortion axis. In forming the self-trapped exciton, the hole is expected to weakly bind an electron [24]. Recombination of the STE contributes to the broad luminescence band of AgCl crystals at low temperatures, which peaks at about 500 nm and originates from the triplet state of STE and recombination in distant pairs formed by a shallow electron center (SEC) and STH, as demonstrated by ODMR [25, 26]. The decay time of the triplet STE in AgCl is ~ 4 ms.

The 95 GHz ODMR spectra measured in AgCl crystal at $B//[100]$ in magnetic field and in zero field by monitoring the luminescence intensity are shown in Fig. 1. An EPR signal corresponding to the triplet to singlet transition was found as shown in Fig. 1a. The resonant transitions and ODMR lines of STE, STH and SEC are marked in (b). The splitting in the zero-field spectrum (c) is attributed to the hyperfine interaction term $A_{zz}S_zI_z$ of the triplet spin with the ^{107}Ag and ^{109}Ag nuclear spins.

As was shown in Refs. [26–28] the positions and the angular dependence of 95 GHz ODMR lines of the STE considerably deviate from those calculated with a simplified $S=1$ spin Hamiltonian, which was used to treat the ODMR data at conventional X- and Q-band frequencies. At the high magnetic field at which the W-band experiments were carried out, the triplet state of the STE cannot be considered as isolated from its accompanying singlet state. In the first high-frequency ODMR experiments the exchange splitting J between the triplet and singlet states of STE was derived, indirectly, via an analysis of the resonance fields of the ODMR transitions by taking into account the magnetic-field-induced mixing between the singlet state ($S=0$) and the triplet state ($M_S=0$) sublevel of the triplet state $S=1$ [27]. This explains why the splitting of the 95 GHz EPR lines of STE in AgCl (Fig. 1b) does not differ by a factor of two in parallel and perpendicular orientations.

The energy levels of recombining electron and hole centers can be described by a spin Hamiltonian

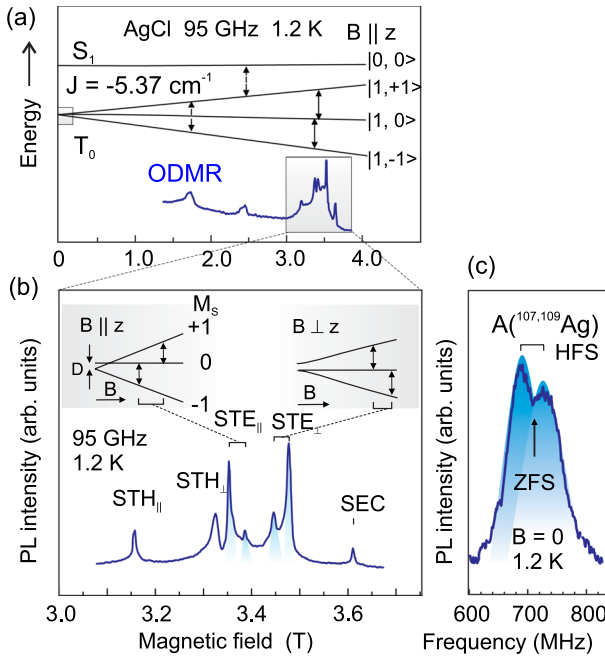


Fig. 1 **a** Energy levels and 95 GHz ODMR transitions of STE in AgCl crystal at $B \parallel [100]$. **b** CW ODMR spectrum of self-trapped excitons (STE), self-trapped hole (STH) and shallow electron center (SEC). **c** Zero-field ODMR spectrum of the STE recorded by scanning the frequency. $T = 1.2$ K

$$\hat{H} = \beta_e \mathbf{B} \cdot \mathbf{g}_e \cdot \mathbf{S}_e + \beta_h \mathbf{B} \cdot \mathbf{g}_h \cdot \mathbf{S}_h + \mathbf{S}_e \cdot \mathbf{D} \cdot \mathbf{S}_h + \mathbf{J} \mathbf{S}_e \cdot \mathbf{S}_h \quad (1)$$

where the first two terms represent the Zeeman interaction of the electron and the hole forming STE. The third term describes the electron–hole spin–spin interaction and the last term describes their exchange interaction. For STE in AgCl \mathbf{D} has axial symmetry with the axis along one of $\langle 100 \rangle$ crystal axes. The principal values of the g -tensor for the hole are $g_{hz} = g_{h\parallel}$ and $g_{hx} = g_{hy} = g_{h\perp}$, the g -factor of the electron g_e is isotropic. Hyperfine interactions are not included.

For distant pairs of recombining centers STH–SEC the exchange interaction $J = 0$ and EPR spectra of individual centers are detected via photoluminescence. Increasing J causes a splitting of the triplet and singlet states. Two different experiments allowed to confirm the existence of the singlet state of STE in AgCl and to measure very precisely the triplet-to-singlet exchange splitting, namely, W-band (95 GHz) ODMR [27, 28] and multiquantum Q-band (35 GHz) ODMR [29, 30].

Numerous multiquantum transitions corresponding to the absorption of up to seven microwave quanta were found in the 35 GHz ODMR spectra of AgCl in a wide magnetic field range from 0.5 to 4 T at a high (> 500 mW) microwave power (see Fig. 2a). A part of the ODMR spectrum with the energy level scheme and EPR transitions corresponding to absorption of n 35 GHz quanta is presented in Fig. 2a. All transitions were unambiguously identified. The assignment of the observed ODMR lines to the multiquantum transitions of the STE was confirmed by ODMR

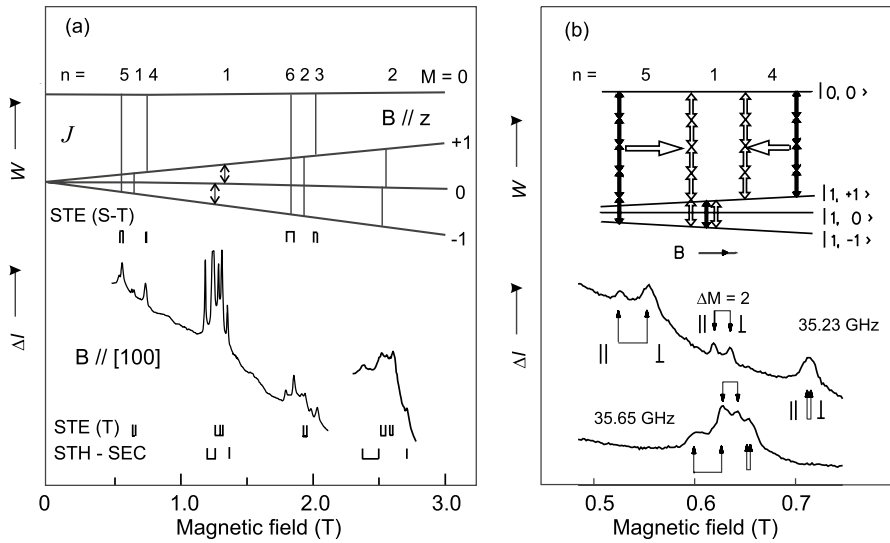


Fig. 2 **a** 35 GHz ODMR spectrum of AgCl crystal measured as variations of the photoluminescence intensity at 1.7 K, $B // [100]$ and microwave power 500 mW. **b** Unambiguous assignment of the multi-quantum transitions corresponding to absorption of 4 and 5 microwave quanta 35 GHz. Arrows show the calculated positions of the corresponding transitions for two values of the microwave frequency

measurements at slightly different microwave frequencies, i.e. with the different energy of the microwave quanta. Two singlet-to-triplet transitions corresponding to the absorption of 4 and 5 microwave quanta are shown in Fig. 2b where the calculated positions of resonances are marked by arrows. Radiofrequency multiphoton resonances were observed in atomic systems in the beginning of the fifties (see [4] and references therein) but in this case the radiofrequency field was not so small as compared to the static magnetic field as in our observations.

Thus, application of high-frequency (95 GHz) and multi-quantum (35 GHz) ODMR allowed to reveal the ordering of the singlet and triplet levels of the STE in AgCl and to measure their splitting with very high accuracy: $|J| = 5.370 \pm 0.002 \text{ cm}^{-1}$.

2.2 ODMR in AgCl and AgBr Nanocrystals

In KCl and KBr crystals heavily doped with silver (1–3%) self-organized AgCl and AgBr nanocrystals are formed [30]. It was found that ODMR spectra of triplet STE in AgCl nanocrystals are different from bulk AgCl, i.e. they have much smaller value of the fine structure splitting parameter D and the g -factor anisotropy for both the isolated STH and the STH forming the STE is substantially reduced (see [31] and references therein). It was supposed that the vibronic coupling at the interface brings about weakening or suppression of the Jahn–Teller effect in sufficiently small-sized nanocrystals ($L < 10 \text{ nm}$ for AgCl in KCl).

Formation of the AgBr nanocrystals in the KBr matrix was confirmed by the appearance of a characteristic peak of the exciton emission in the luminescence

spectra and its blue shift relative to the exciton emission in bulk AgBr, which appears because of spatial confinement effects. 35 GHz ODMR spectra of bulk AgBr and AgBr nanocrystals are compared in Fig. 3a.

In bulk AgBr, the ODMR spectrum is dominated by the lines of the SEC at $g=1.49$ and the localized holes (h) at $g=2.08$. The shape of the ODMR line of shallow donors in bulk semiconductors is usually analyzed from the point of view of exchange interactions in recombining donor–acceptor pairs with a random distribution of interpair distances. The shape of the ODMR spectrum of SEC in AgBr nanocrystals (highlighted in (a)) can also be accounted for by a distribution of interpair separations in recombining electron–hole pairs and the corresponding distribution of the exchange splittings J . Since the maximum separation between the recombining centers is limited to the nanocrystal size, there exist no distant pairs in nanocrystals. Therefore, the minima of the ODMR amplitude are expected at the magnetic fields corresponding to g -factors of the isolated SEC and hole centers. The resonance fields B corresponding to the EPR transitions at 35.2 GHz, calculated using the spin Hamiltonian Eq. (1) for various exchange interactions J in the recombining pairs of hole centers ($g=2.08$) and SEC ($g=1.57$), as well as the relative number N of the recombining pairs as a function of J , obtained from the shape of the ODMR spectrum, are shown in Fig. 3b. With the assumption that J depends exponentially on the interpair separation and with the Bohr radius of SEC measured by ENDOR [25], the interpair separation can be obtained from the value of J . Supposing that the center of the

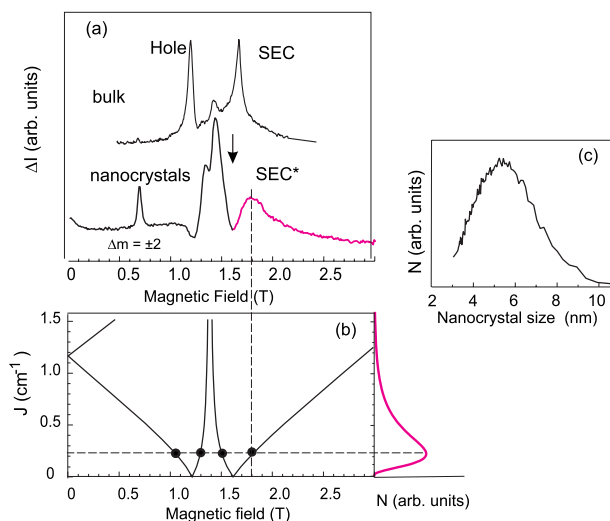


Fig. 3 **a** ODMR spectrum recorded by monitoring the microwave-induced variations of the total emission of bulk AgBr crystals and AgBr nanocrystals in KBr. $T=1.8$ K; $\nu=35.2$ GHz; $P=300$ mW; $f_m=80$ Hz. **b** Resonance fields B corresponding to the EPR transitions at 35.2 GHz calculated as a function of the exchange splitting J for a pair of the recombining centers with spins $1/2$ and g values of 2.08 (a hole) and 1.57 (an electron). The right-hand curve shows the relative number N of the recombining pairs as a function of J determined from the ODMR spectrum. **c** Size distribution of AgBr nanocrystals obtained from the ODMR spectrum

wave function of SEC is located at the center of the nanocrystal and the holes are localized near the interface, the size distribution of the AgBr nanocrystals in KBr was obtained [32, 33]. The size distribution of AgBr nanocrystals in the sample under study is shown in Fig. 12c. The mean nanocrystal size is estimated to be about 5.5 nm, which is in good agreement with the estimates made on the basis of the blue shift of the exciton emission peak.

2.3 Electron-Nuclear Double Resonance and the Wave-Function Distribution of STE in AgCl

STE in AgCl were studied by electron spin echo (ESE) [26]. ESE-detected EPR spectrum and electron-nuclear double resonance (ENDOR) of STE and SEC in undoped AgCl crystal are shown in Fig. 4. The ESE-detected EPR (Fig. 4a) is obtained by monitoring the amplitude of the ESE signal created at time τ after a $(\pi/2) - \tau - \pi$ microwave pulse sequence. The $\pi/2$ pulse length is 100 ns, $\tau = 650$ ns, and the repetition rate of the pulse sequence is 33 Hz. The electron-nuclear double resonance (ENDOR) spectra (Fig. 4b) were recorded at 94.9 GHz and 1.2 K with B along the cubic axis, which is perpendicular to the distortion axis of the STE (STE_{\perp}): the upper spectrum was obtained by monitoring the high-field EPR transition of STE_{\perp} , which corresponds to the transition between the $M_S = 0$ and $M_S = -1$ sublevels of the triplet, and the lower spectrum was recorded via the low-field transition of STE_{\perp} , which corresponds to the transition between $M_S = 0$ and $M_S = +1$. Typical pulse lengths were: $\pi/2 = 100$ ns, τ between 400 and 900 ns, $T = 700$ μ s and the length of radio-frequency (RF) pulse = 600 μ s.

ENDOR studies of SEC were presented in Ref. [34]. The dynamical properties of the excited singlet and triplet states of the STE were studied in Ref. [28].

Figure 5 shows the radial dependence describing of the electronic part of the envelope function of STE (a) and the density of the envelope function of SEC (b) in AgCl. The ENDOR study has demonstrated that the lowest triplet state of the STE consists of a very diffuse electron attracted by a strongly localized STH [35]. The spatial distribution of the STE can roughly be divided into three regions. At distances larger than about 18 Å, the wave function of the STE is completely determined by the shallow electron, which occupies a hydrogen-like 1s orbital. At distances between 18 and 9 Å, the electron is still dominant but its density distribution deviates from the spherical symmetry and reflects the D_{4h} symmetry of the central STH. At distances shorter than about 9 Å, both the central hole and the shallow electron have a contribution to the wave function of the STE.

The electron in STE is mainly contained in a hydrogen-like 1s orbital with a Bohr radius of 15.160 Å, but near its center the electron density deviates from spherical symmetry and reflects the D_{4h} charge distribution of the hole. From a comparison with the results of an ENDOR study of the self-trapped hole, it is concluded that the microscopic and electronic structure of a self-trapped hole is not significantly altered by the attraction of a shallow electron [26].

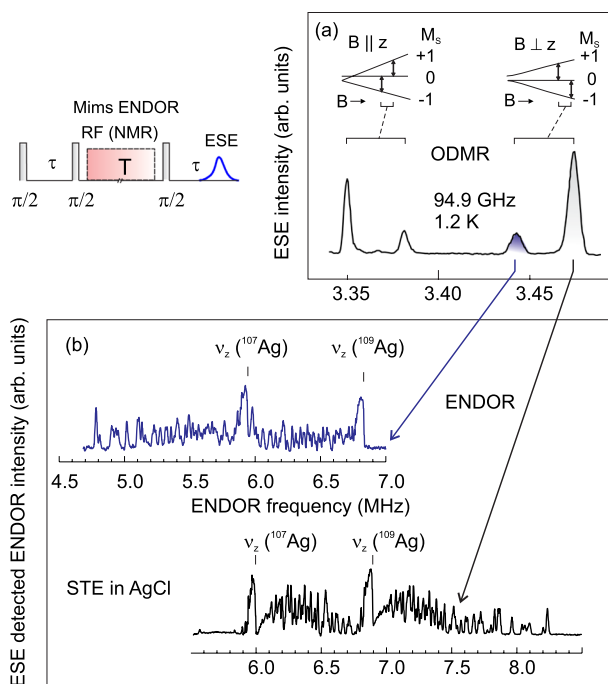


Fig. 4 **a** ESE-detected EPR spectrum of STE in undoped AgCl crystal recorded with $B \parallel [001]$ at 94.9 GHz and 1.2 K, during continuous UV irradiation. **b** ENDOR spectra in the triplet state of the STE in AgCl

3 ODMR and Level Anticrossings of Heavy-Hole Excitons in GaAs/AlAs Superlattices

In GaAs/AlAs superlattice (SL), both type-II and type-I band ordering can be obtained [36].

Excitons are formed by an electron with spin $S = 1/2$ and a heavy hole (hh) with $M_j = \pm 3/2$. In type-I structures, the electron and the hole are both confined in the same GaAs layer. In type-II SL the electrons and the holes are spatially separated in the adjacent AlAs in GaAs layers, respectively, and their envelope functions overlap at interfaces. Excitons that are formed by these electrons and holes recombine at the interfaces and are very sensitive to the interface microstructure.

A transmission electron-microscopy (TEM) micrograph of a cross-section of a typical SL is shown in Fig. 6a. The type of band ordering depends on the GaAs and AlAs layer thickness. This is illustrated by map shown in Fig. 6b. Insets show the valence and conduction band structure of type-II and type-I regions and exciton recombination transitions. X and Γ denote the states of holes (solid lines) and electrons (dashed lines). Position of the sample E913 that was especially grown with a composition gradient is also shown. In this SL a transition between type-II

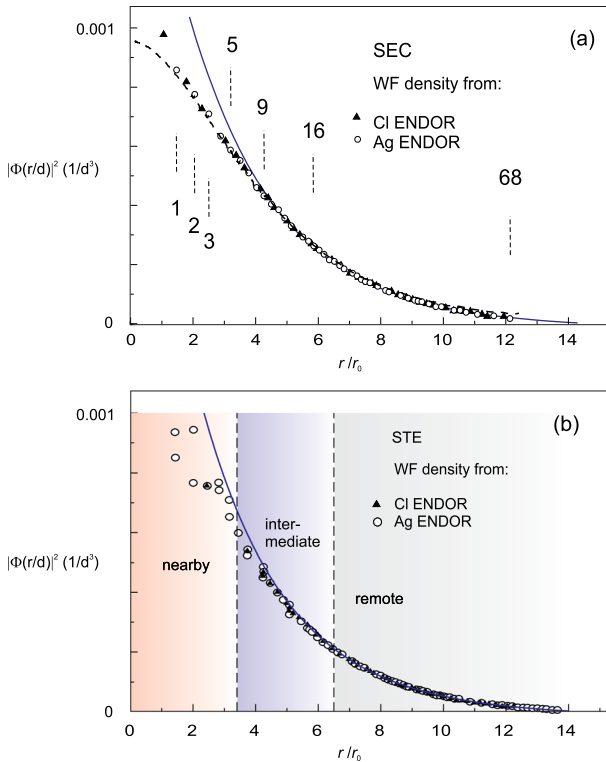


Fig. 5 The radial dependence of the density of the envelope function describing the shallow electron center (a) and the electronic part of self-trapped exciton (b). The regions of the three classes of nuclei are marked. Most of the indicated densities are derived from the silver ENDOR spectrum, however, in the remote region and part of the intermediate region densities obtained from the chlorine ENDOR spectrum are included. The solid line illustrates the exponential radial dependence in the remote region. The interionic lattice distance d equals 2.7532 \AA at 0 K

and type-I band ordering can be monitored simply by changing position of the excitation spot on the sample.

The lifetime of hh-excitons in type-II SLs is of the order of microseconds and ODMR can be easily observed [37, 38]. The energy levels and EPR transitions corresponding to the hole and electron spin flips in the hh-exciton are shown Fig. 7a. In the low field regions strong signals of the exciton level anticrossing (LAC) are detected. ODMR studies of a number of type-II SLs showed that the exchange splitting Δ of hh-excitons depends mainly on the SL period and increases with decreasing period [30].

Variations of the ODMR and LAC signals measured at different points of the sample E913 grown with the composition gradient are presented in Fig. 7b. One can see that in the type-II-type-I transition region ODMR signals disappear and LAC signals shift to much higher fields. The disappearance of ODMR is explained by a decrease in the exciton lifetime below 100 ns and the shift of LAC signals

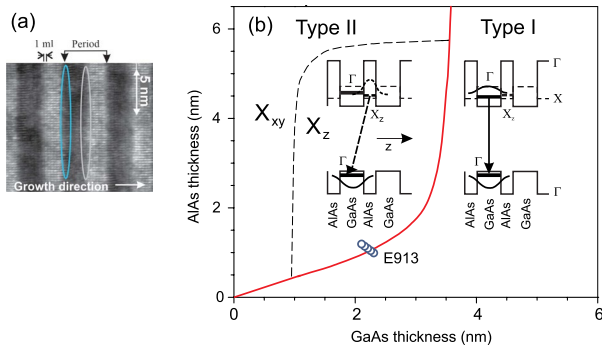


Fig. 6 **a** Cross-sectional TEM photograph of an MBE grown type-II GaAs/AlAs SL. The excitons can be localized at one of the opposite interfaces. **b** Map displaying the border between type-I SLs and type-II SLs with the lowest conduction band states X_z and X_{xy} . Insets show the valence and conduction band structure of type-II and type-I GaAs/AlAs superlattice. Thin lines show energy of Γ (solid lines) and X (dashed lines) states in the bulk materials, thick lines correspond to the superlattice states

corresponds to an increase in the exchange splitting for type-I excitons. Since the LAC is not connected with microwave-induced transitions it can be observed for excitons with lifetimes in the nanosecond range that is typical for type-I SLs [30, 39].

The two radiative levels of type-II exciton are split in zero field into $[110]$ or $[\bar{1}\bar{1}0]$ dipoles and the order of these levels depends on the type of the interface—direct

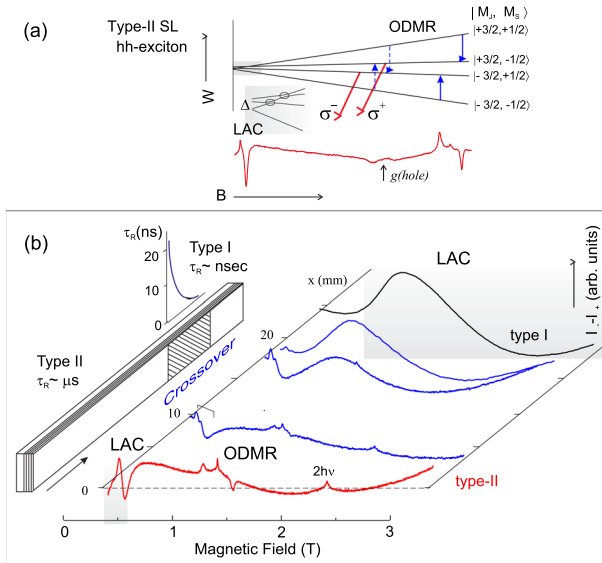


Fig. 7 **a** Energy levels and resonance transitions in a type-II GaAs/AlAs SL together with the ODMR spectrum recorded by monitoring circular polarization of luminescence. **b** ODMR and LAC signals measured at different points of the sample E913 grown with the composition gradient. One can see that in the type-II–type-I transition region ODMR signals disappear and LAC signals shift to higher fields

(AlAs on GaAs) or inverted (GaAs on AlAs) [36, 40]. Measurements of LAC in linear polarization of luminescence in two specially designed type-II SLs, in which recombination occurs at one of the opposite interfaces, it was established that the lowest excitonic radiative level has $[110]$ symmetry at the direct interface and $[\bar{1}\bar{1}0]$ symmetry at the inverted interface [41, 42]. This allowed to analyze interfaces in different type-II SLs and to study exciton localization depending on the growth conditions.

Measurements of LAC in linear polarization of luminescence in type-II SLs showed that LAC signals from two classes of excitons appear in different magnetic fields. This implies that the excitons localized at opposite interfaces differ in the exchange splitting as shown in Fig. 8.

This is caused by the asymmetric composition profiles of the opposite interfaces [43]. Due to different surface segregation rates of Ga and Al, Ga penetrates into the AlAs layers forming the saw-like composition profile shown in Fig. 8a. The calculated band structure for excitons recombining at the opposite interfaces is presented in Fig. 8b. Figure 8c shows LAC signals (thick black line) and the result of decomposition into LAC of excitons recombining at direct and inverted interfaces (thin lines) together with the corresponding energy level schemes.

4 NV Centers in Diamond

A nitrogen-vacancy (NV) defect in diamond is a complex consisting of a nitrogen atom replacing carbon in the diamond lattice and a vacancy in an adjacent site (Fig. 9a). Diamond with NV defects was the first solid-state system where manipulation of the single spin was realized at room temperature [44–46] and is actually widely studied. Upon optical excitation a strong spin alignment, i.e. spin

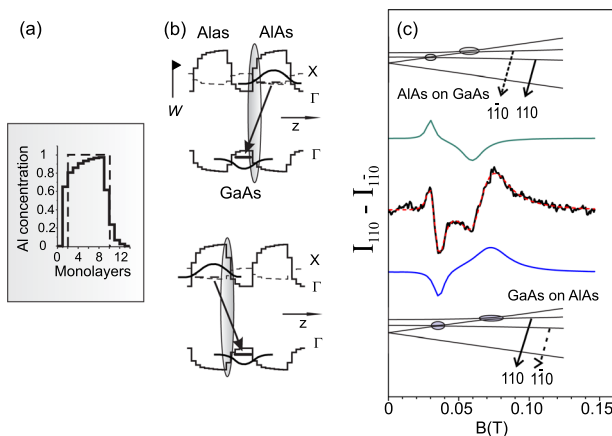


Fig. 8 **a** Composition profile of AlAs layer grown on GaAs. **b** Calculated band structure of GaAs/AlAs SL and two classes of exciton recombination. **c** Linearly polarized luminescence in magnetic field (thick black line), its decomposition into LAC of excitons recombining at opposite interfaces and corresponding energy level schemes

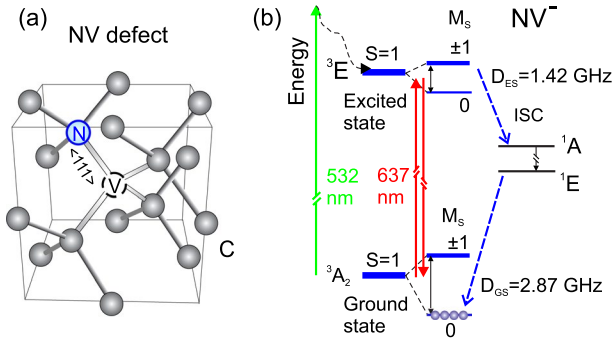


Fig. 9 The structure and the optical pumping cycle of NV center in diamond

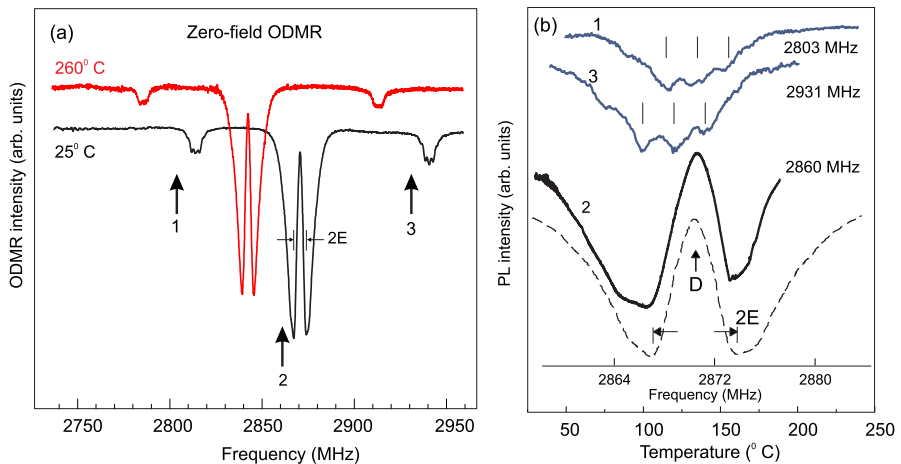


Fig. 10 **a** Zero-field ODMR spectra of the NV defects and the NV–Ns pairs, recorded in zero magnetic field at 25 °C and 260 °C. Arrows mark the values of frequencies at which temperature-scanned ODMR spectra shown in **b** were recorded. For comparison dashed line in **b** shows the central part of the usual ODMR spectrum ODMR at $T = 25$ °C

polarization of the center into the $m_s = 0$ sublevel through optical pumping, is generated in the triplet ($S = 1$) ground state 3A_2 with the zero-field splitting (ZFS) of 2870 MHz due to spin selective shelving into a metastable state 1A_1 (Fig. 9b). Due to the strong thermal isolation of the NV defect spin system from the diamond lattice, the spin–lattice relaxation does not strongly influence the non-equilibrium distribution of the spin sublevel populations generated by the optical pumping. As a result, ODMR both in the ground and excited states of the NV defect can be observed by monitoring the photoluminescence (PL) intensity. However, short lifetime of the excited state requires high microwave power for ODMR measurements [6]. NV defect in diamond is one of the most prominent objects for quantum information applications [47].

In Ref. [48] the temperature dependence of the axial zero-field splitting parameter, D , of the NV defect ensemble was observed. The temperature induced effects provide an opportunity to develop a new method of magnetic resonance detection [49]. Figure 10a shows the ODMR spectra of the NV–Ns pairs recorded at zero magnetic field at 25 and 250 °C. ODMR recorded at $B=0$ and fixed frequency by scanning temperature from 25 to 250 °C is shown in Fig. 10b. The values of fixed frequencies are marked by arrows in (a) and are indicated in (b). The central part of a conventional ODMR spectrum measured at 25 °C is shown in (b) for comparison. These measurements allowed concluding that all these spectra belong to the same paramagnetic molecular system—the fact that is not obvious from the standard ODMR measurements.

5 Silicon Vacancy Related Defects in SiC

The unique quantum properties of NV-centers in diamond have motivated efforts to find defects with similar properties in silicon carbide (SiC), which can extend the functionality of such systems. Atomic-scale defects in bulk and nanocrystalline SiC are promising for quantum information processing, photonics, and sensing [50]. There are two families of spin centers in SiC with unique mechanism of an optical spin alignment of the spin sublevels. The first family, is a silicon-carbon divacancy of the neighboring positions with covalent molecular bond and having a triplet ground state ($S=1$). The second family of the centers, is a negatively charged silicon vacancy V_{Si} in the paramagnetic state that is bonded to the neutral carbon vacancy V_C^0 in the non-paramagnetic state, located on the adjacent site along the SiC symmetry c axis and having quartet ground and excited states ($S=3/2$). They exhibit unique characteristics such as optical spin alignment up to 250 °C [51–57]. Depending on the temperature, crystal polytype, and crystal position, two opposite schemes have been observed for the optical alignment of the populations of the spin sublevels of the high-spin ground state of the Si vacancy in SiC upon irradiation with unpolarized light at the zero-phonon lines (ZPLs) [50]. The structure of some vacancy-related $S=3/2$ centers in four polytypes of SiC is shown in Fig. 11. The V2 center is highlighted and will be discussed below.

Zero-field ODMR spectrum of V2 center 4H-SiC recorded by monitoring luminescence intensity is shown in Fig. 12a. The two peaks belong to the ground state (GS) with zero field splitting of about 70 MHz and the excited state (ES) with zero field splitting of about 410 MHz [58]. To observe ODMR in the excited state it was necessary to apply a very high rf power (40 dBm) since the radiative lifetime of the excited state is several nsec. It was found that the ES splitting strongly increases with decreasing temperature whereas the GS splitting does not change as shown in Fig. 12b. Although there is still no complete explanation for this effect, it can be assumed that it arises due to thermal expansion of the lattice. The difference in the behavior of ES and GS splittings may be due to the different spatial extension of these states.

Figure 13a shows the energy levels and LAC points for both the ground and excited states of V2 centers in 6H-SiC. Transitions from the excited state 4E to

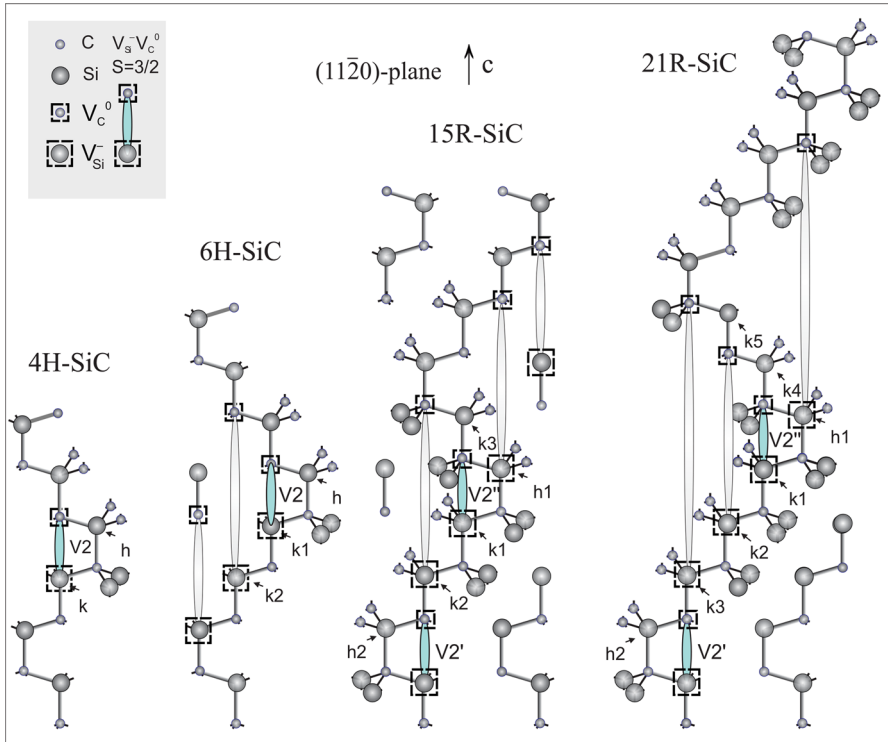


Fig. 11 Fragments of crystal lattice of four SiC polytypes: hexagonal 4H-SiC and 6H-SiC and rhombic 15R-SiC and 21R-SiC. The plane of the drawing coincides with the $(11\bar{2}0)$ crystal plane. A possible model—the spin center family is shown: these spin centers have quadruplet spin ground and excited states with $S = 3/2$. V2 centers which will be considered below are highlighted

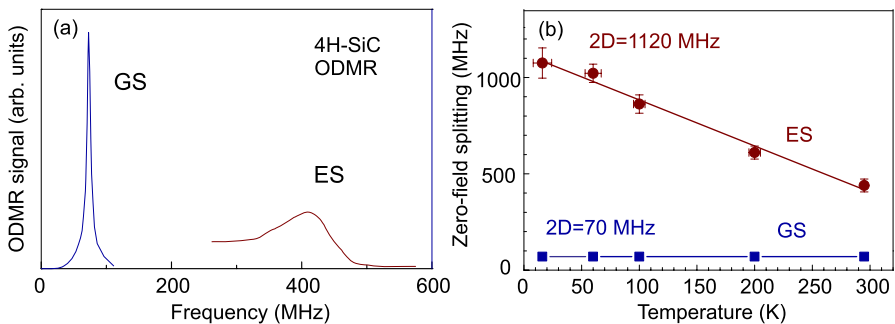


Fig. 12 **a** ODMR spectrum of V2 center in 4H-SiC at zero magnetic field at RT. The two peaks belong to the ground state (GS) zero field splitting at around 70 MHz and the excited state (ES) zero field splitting at around 410 MHz [59]. **b** Temperature dependence of the zero-field spin splittings in the ground and excited states obtained from the ODMR measurements. $2D = 1120\text{--}2.4$ MHz/K

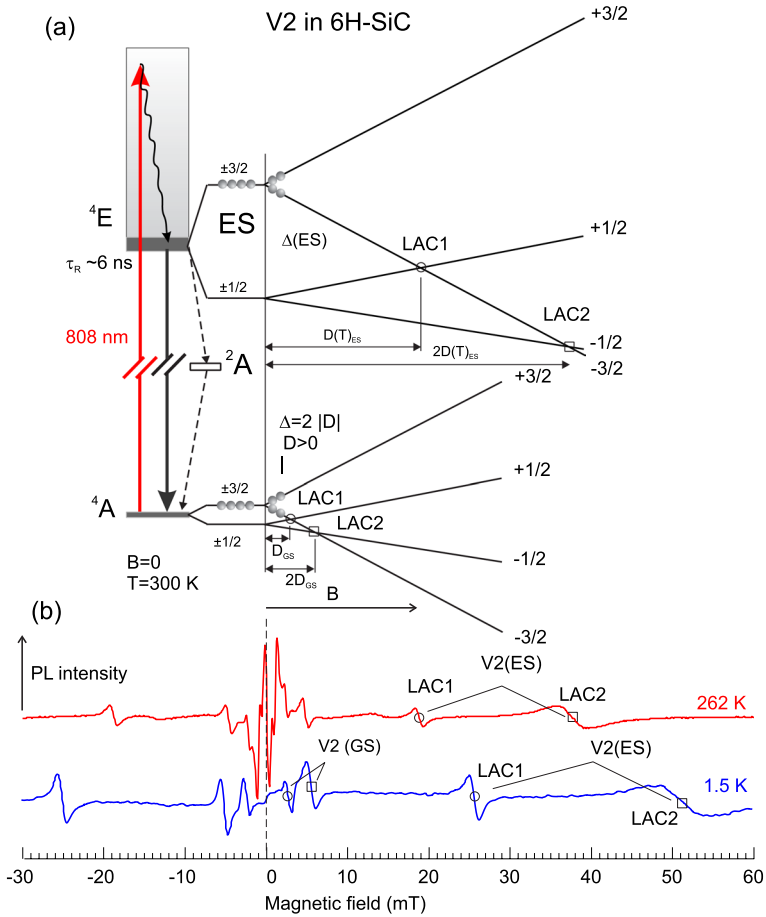


Fig. 13 **a** Optical pumping scheme and energy levels in magnetic field for V2 centers in 6H-SiC. LAC points are marked. **b** LAC signals of the ground and excited states of V2 defects in 6H-SiC recorded with modulation of magnetic field. The positions of the excited state LAC signals depend on temperature because of the temperature dependence of the zero-field splitting

the ground state 4A can occur through two ways: (1) the radiative transition with spin conservation in the form of phosphorescence, which is shown in the upper part of Fig. 13, and (2) the nonradiative transition without spin conservation from the excited state 4E to an intermediate metastable state (the so-called intersystem crossing) with the subsequent transition from the metastable state to the ground state 4A . In this case, since the transitions are spin-selective, the populations of the spin center are aligned after several cycles of optical excitation (usually, within a sub-microsecond time interval). In particular, for V2 in 6H-SiC, lower levels with $S = \pm 1/2$ are populated, whereas the levels with $S = \pm 3/2$ are depleted. The lifetime in the excited state is ~ 6 ns.

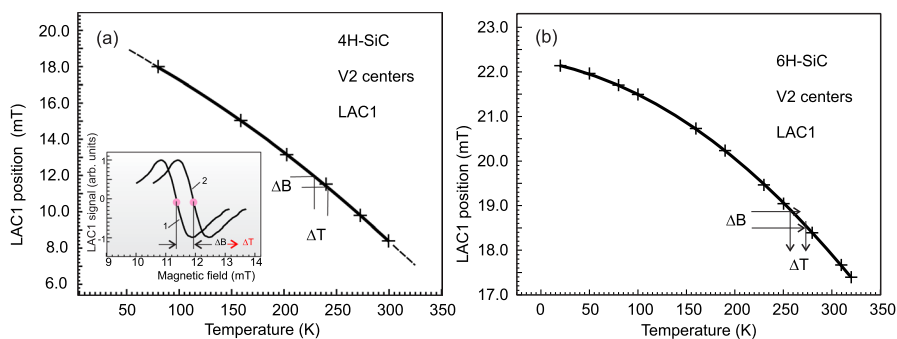


Fig. 14 Temperature dependence of positions of the excited state LAC signals of V2 centers in 4H-SiC (a) and 6H-SiC (b). Inset in a illustrates the use of LAC for temperature sensing

LAC signals of the ground and excited states of V2 defects in 6H-SiC measured at 1.5 K and 262 K are shown in Fig. 13b. The ES LAC lines shift to lower fields with increasing temperature. This implies that in 6H-SiC the zero-field splitting in ES of V2 centers decreases with temperature similar to 4H-SiC. Temperature dependences of the zero-field splitting in the excited state of V2 centers in 4H- and 6H-SiC are shown in Fig. 14a, b, respectively.

Both ODMR and LAC in the excited state of vacancy-related centers in SiC can be used for temperature sensing with spatial resolution. The detection of the ODMR signal may be difficult because it would require the application of highly intense rf fields. On the contrary, a variation of the photoluminescence (PL) intensity at LAC when the ODMR signal is not detectable has been clearly demonstrated using GaAs/AlAs superlattices. Observation of LAC is much easier than ODMR, it does not require strong microwave field that produce additional heating of the sample. The use of LAC allows temperature to be measured entirely optically. In addition, it allows to study large samples and to scan them with a high spatial resolution using confocal microscopes.

In 15R-SiC cross-relaxation resonances (CRR) were observed via PL intensity at room temperature in addition to LAC signals [57]. Figure 15 illustrates a possibility of all-optical quantum thermometry based on cross-relaxation of spin-levels of a “bright” $S=3/2$ center with a “dark” $S=1$ center and multicenter entanglement under ambient conditions in 15R-SiC. Besides the ground state (GS) and excited state (ES) LACs additional lines were found at magnetic fields above 16 mT. These resonances lines are much narrower as compared to LAC and also shift to higher fields with increasing temperature. A possible explanation for the nature of these lines is cross-relaxation with other paramagnetic centers in the crystal (e.g., centers with $S=1$ [57, 58, 60]), for which optical pumping at room temperature does not create a population inversion. As a result, these centers have different spin temperatures and a cross-relaxation process between the spin levels of $S=3/2$ centers and the triplet center is observed. Considering the narrowness of the CRR lines, this effect can be used for a purely all-optical thermometry.

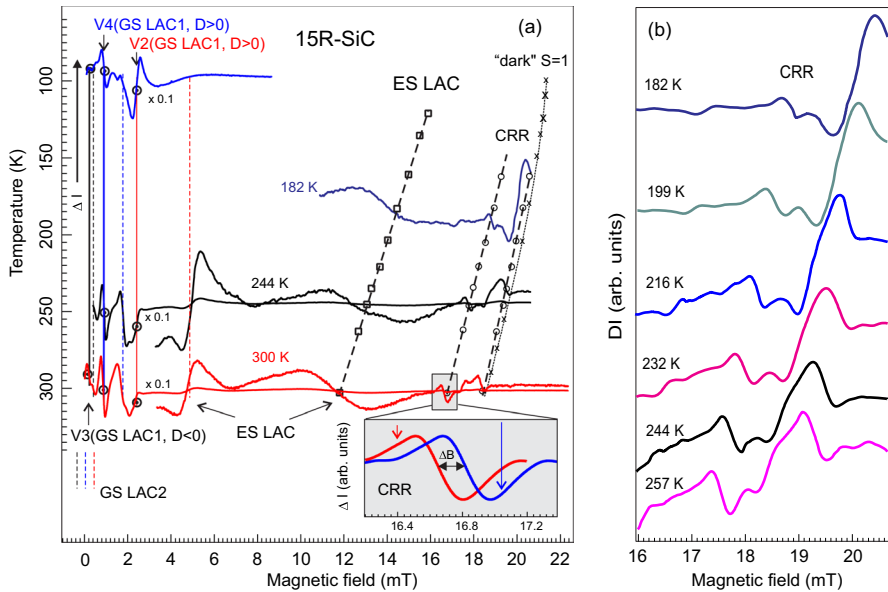


Fig. 15 **a** Variations of the luminescence intensity vs magnetic field measured in 15R-SiC at different temperatures. Temperature dependence of LAC in the excited state of V2 defect in 15R-SiC and cross-relaxation signals is shown by dashed lines. **b** Temperature dependence of cross-relaxation resonance (CRR) signals in extended scale

Measuring local temperature with a spatial resolution on the order of a few nanometers has a wide range of applications in the semiconductor industry and in material and life sciences. For example, probing temperature on the nanoscale with high precision can potentially be used to detect small, local temperature changes like those caused by chemical reactions or biochemical processes. Application of LAC in the excited state and cross-relaxation resonances of vacancy-related defects in SiC seems to be promising for all-optical thermometry with high spatial resolution.

6 Conclusions

ODMR emerged as a method for studying excited states using magnetic resonance. It has been widely used to investigate excited states of intrinsic and impurity defects and excitons in ionic crystals and semiconductors, as well as in nanostructures based on them, to investigate triplet excited states in organic molecules, to elucidate the nature of spin-dependent recombination. It has now developed into a powerful, highly sensitive method for probing and manipulating single spins.

We have outlined the several representative examples of the use of magnetic resonance spectroscopy to study excited states: (1) ODMR, ESE, ENDOR in the excited state of self-trapped excitons in ionic-covalent silver halides crystals and nanocrystals. (2) ODMR and LAC spectroscopy of localized heavy-hole excitons

in semiconductor quantum wells and superlattices. (3) LAC and ODMR in excited states of spin centers in diamond and silicon carbide.

Application of LAC and cross-relaxation spectroscopy seems to be especially useful for applications of short-lived excited states in all-optical sensing with spatial resolution.

Acknowledgements This work was supported by the Russian Science Foundation (project no. 23-12-00152, <https://rscf.ru/project/23-12-00152>).

Author Contributions P.B., R.B. and N.R. wrote the mail manuscript text and prepared figures. R.B. and N.R. reviewed the manuscript.

Data Availability No datasets were generated or analysed during the current study.

Declarations

Conflict of interest The authors declare no competing interests.

References

1. J. Brossel, A. Kastler, *Compt. Rend.* **229**, 1213 (1949)
2. J. Brossel, F. Bitter, *Phys. Rev.* **86**, 308 (1952)
3. A. Kastler, *J. Phys. Radium* **11**, 255–265 (1950)
4. C. Cohen-Tannoudji, *Compt. Rend. Physique* **20**, 658–670 (2019). <https://doi.org/10.1016/j.crhy.2019.01.001>
5. S. Geschwind, G.E. Devlin, R.L. Cohen, S.R. Chinn, *Phys. Rev.* **137**, A1087 (1965)
6. P. Neumann, R. Kolesov, V. Jacques, J. Beck, J. Tisler, A. Batalov, L. Rogers, N.B. Manson, G. Balasubramanian, F. Jelezko, J. Wrachtrup, *New J. Phys.* **11**, 013017 (2009)
7. N. Mathur, A. Mukherjee, X. Gao, J. Luo, B.A. McCullian, T. Li, A.N. Vamivakas, G.D. Fuchs, *Nat. Commun.* (2022). <https://doi.org/10.1038/s41467-022-30772-z>
8. S. Geshwind, in *Electron Paramagnetic Resonance*. ed. by S. Geshwind (Plenum, New York, 1972), pp.353–426
9. M. Sharnoff, *J. Chem. Phys.* **46**, 3263 (1967)
10. J. Schmidt, J.H. Van der Waals, *Chem. Phys. Lett.* **2**, 640 (1968)
11. R.H. Clarke, *Triplet State ODMR Spectroscopy: Techniques and Applications to Biophysical Systems* (Wiley, New York, 1982)
12. D. Carbonera, *Photosynth. Res.* **102**, 403 (2009). <https://doi.org/10.1007/s11120-009-9407-5>
13. R. Romestain, L.S. Dang, Y.M. d'Aunigné, A. Fukuda, *Semicond. Insul.* **3**, 175 (1978)
14. P.G. Baranov, Yu.P. Veshchunov, V.A. Vetrov, N.G. Romanov, *Fiz. Tverd. Tela (St. Petersburg)* **23**, 2900 (1981)
15. R.T. Williams, M.N. Kabler, W. Hayes, J.P. Stott, *Phys. Rev. B* **14**, 725 (1976)
16. N.G. Romanov, V.A. Vetrov, P.G. Baranov, *Pis'ma Zh. Eksp. Teor.* **37**, 325 (1983)
17. B.C. Cavanett, *Adv. Phys.* **4**, 475 (1981). <https://doi.org/10.1080/00018738100101397>
18. P.G. Baranov, Yu.P. Veshchunov, P.G. Baranov, *Fiz. Tverd. Tela (St. Petersburg)* **25**, 3299 (1983)
19. J. Grüne, V. Dyakonov, A. Sperlich, *Mater. Horiz.* **8**, 2569 (2021). <https://doi.org/10.1039/d1mh00999k>
20. L.F. Mollenauer, G. Baldacchini, *Phys. Rev. Lett.* **29**, 465 (1972)
21. Y. Ruedin, P.-A. Schnegg, C. Jaccard, M.A. Aegerter, *Phys. Stat. Solids (b)* **54**, 565 (1972)
22. N.G. Romanov, Yu.P. Veshchunov, V.A. Vetrov, P.G. Baranov, *Phys. Stat. Solids (b)* **110**, 89 (1982)
23. V.G. Panov, A.N. Varaksin, A.B. Sobolev, *Phys. Solid State* **50**, 1028 (2008)
24. W. von der Osten, in *Physics of II–VI and I–VII Compounds, Semimagnetic Semiconductors, Landolt-Börnstein, New Series, Group 17*, vol. 17, Pt. b, ed. by K.-H. Hellwege, O. Madelung (Springer, Berlin, 1982)
25. J.P. Spoonhower, F.J. Ahlers, R.S. Eachus, W.G. McDugle, *J. Phys. Condens. Matter* **2**, 3021 (1990)
26. P.G. Baranov, N.G. Romanov, O.G. Poluektov, J. Schmidt, *Appl. Magn. Reson.* **39**, 453–486 (2010). <https://doi.org/10.1007/s00723-010-0180-6>

27. M.C.J.M. Donckers, O.G. Poluektov, J. Schmidt, P.G. Baranov, Phys. Rev. B **45**, 13061 (1992)
28. O.G. Poluektov, M.C.J.M. Donckers, P.G. Baranov, J. Schmidt, Phys. Rev. B **47**, 10226 (1993)
29. N.G. Romanov, P.G. Baranov, Semicond. Sci. Technol. **9**, 1080 (1994). <https://doi.org/10.1088/0268-1242/9/5/012>
30. P.G. Baranov, N.G. Romanov, Appl. Magn. Reson. **21**, 165 (2001). <https://doi.org/10.1007/BF03162450>
31. P.G. Baranov, V.S. Vikhnin, N.G. Romanov, V.A. Khramtsov, J. Phys. Condens. Matter **13**, 2651 (2001). <https://doi.org/10.1088/0953-8984/13/11/320>
32. P.G. Baranov, N.G. Romanov, V.L. Preobrazhenski, V.A. Khramtsov, JETP Lett. **76**, 465 (2002)
33. P.G. Baranov, N.G. Romanov, V.A. Khramtsov, V.S. Vikhnin, Nanotechnology **12**, 540 (2002). <https://doi.org/10.1007/s00723-010-0180-6>
34. M.T. Bennebroek, A. Arnold, O.G. Poluektov, P.G. Baranov, J. Schmidt, Phys. Rev. B **54**, 11276 (1996)
35. M.T. Bennebroek, A. Arnold, O.G. Poluektov, P.G. Baranov, J. Schmidt, Phys. Rev. B **53**, 15607 (1996)
36. E.L. Ivchenko, G.E. Pikus, in *Superlattices and Heterostructures. Symmetry and Optical Phenomena, Springer series in Solid State Sciences*, vol. 110, ed. by M. Cardona (Springer, Berlin, 1997)
37. H.W. Van Kesteren, E.C. Cosman, W.A.J.A. Van der Pool, C.T. Foxon, Phys. Rev. B **41**, 5283–5292 (1990)
38. P.G. Baranov, I.V. Mashkov, N.G. Romanov, P. Lavallard, R. Planel, Solid State Commun. **87**, 649–654 (1993)
39. N.G. Romanov, P.G. Baranov, Nanotechnology **12**(2001), 585–590 (2001)
40. I.L. Aleiner, E.L. Ivchenko, JETP Lett. **55**, 692 (1992)
41. P.G. Baranov, I.V. Mashkov, N.G. Romanov, C. Gourdon, P. Lavallard, R. Planel, Pis'ma Zh. Eksp. Teor. Fiz. **60**, 429 (1994). (JETP Lett. **60**, 445 (1994))
42. C. Gourdon, I.V. Mashkov, P. Lavallard, Phys. Rev. B **57**, 3955 (1998)
43. P.G. Baranov, N.G. Romanov, A. Hofstaetter, A. Scharmann, C. Schnorr, F.J. Ahlers, K. Pierz, JETP Lett. **64**, 754–759 (1996)
44. A. Gruber, A. Drabenstedt, C. Tietz, L. Fleury, J. Wrachtrup, C. von Borczyskowski, Science **276**, 2012–2014 (1997)
45. F. Jelezko, I. Popa, A. Gruber et al., Appl. Phys. Lett. **81**, 2160 (2002)
46. P. Nizovtsev, S.Y. Kilin, F. Jelezko et al., Phys. B Condens. Matter **340–342**, 106 (2003)
47. J. Wrachtrup, Proc. Natl. Acad. Sci. U.S.A. **107**, 9479 (2010)
48. V.M. Acosta, E. Bauch, M.P. Ledbetter et al., Phys. Rev. Lett. **104**, 070801 (2010). <https://doi.org/10.1103/PhysRevLett.104.070801>
49. R.A. Babunts, A.A. Soltamova, D.O. Tolmachev, V.A. Soltamov, A.S. Gurin, A.N. Anisimov, V.L. Preobrazhenskii, P.G. Baranov, JETP Lett. **95**, 429 (2012). <https://doi.org/10.1134/S0021364012080024>
50. P.G. Baranov, H.J. Von Bardeleben, F. Jelezko, J. Wrachtrup, *Magnetic Resonance of Semiconductors and Their Nanostructures* (Springer, Vienna, 2017), p.484. <https://doi.org/10.1007/978-3-7091-1157-4>
51. P.G. Baranov, A.P. Bundakova, A.A. Soltamova, S.B. Orlinskii, I.V. Borovykh, R. Zondervan, R. Verberk, J. Schmidt, Phys. Rev. B **83**, 125203 (2011)
52. P.G. Baranov, V.A. Soltamov, A.A. Soltamova, G.V. Astakhov, V.V. Dyakonov, in: *Silicon Carbide and Related Materials*, Mater. Sci. Forum, vol. 740–742, pp. 425–430 (2013)
53. V.A. Soltamov, B.V. Yavkin, D.O. Tolmachev, R.A. Babunts, A.G. Badalyan, VYu. Davydov, E.N. Mokhov, I.I. Proskuryakov, S.B. Orlinskii, P.G. Baranov, Phys. Rev. Lett. **115**, 247602 (2015)
54. D. Simin, V.A. Soltamov, A.V. Poshakinskiy, A.N. Anisimov, R.A. Babunts, D.O. Tolmachev, E.N. Mokhov, M. Trupke, S.A. Tarasenko, A. Sperlich, P.G. Baranov, V. Dyakonov, G.V. Astakhov, Phys. Rev. X **6**, 031014 (2016)
55. A.N. Anisimov, D. Simin, V.A. Soltamov, S.P. Lebedev, P.G. Baranov, G.V. Astakhov, V. Dyakonov, Nat. Sci. Rep. **6**, 33301 (2016)
56. A.N. Anisimov, R.A. Babunts, S.V. Kidalov, E.N. Mokhov, V.A. Soltamov, P.G. Baranov, JETP Lett. **104**, 82–87 (2016)
57. G.V. Astakhov, D. Simin, V. Dyakonov, B.V. Yavkin, S.B. Orlinskii, I.I. Proskuryakov, A.N. Anisimov, V.A. Soltamov, P.G. Baranov, Appl. Magn. Reson. **47**, 793–812 (2016)
58. S.A. Tarasenko, A.V. Poshakinskiy, D. Simin, V.A. Soltamov, E.N. Mokhov, P.G. Baranov, V. Dyakonov, G.V. Astakhov, Phys. Status Solidi B **00**, 17002582017 (2018). <https://doi.org/10.1002/pssb.201700258>
59. V.S. Vainer, V.A. Il'in, Sov. Phys. Solid State **23**, 2126 (1981). ([*Fiz. Tverd. Tela* **23**, 3659 (1981)])
60. N.M. Pavlov, M.I. Iglitsyn, M.G. Kosaganova, V.N. Solomatina, Sov. Phys. Semicond. **9**, 845 (1975). ([*Fiz. Tekh. Poluprovodn.* **9**, 1279 (1975)])

Publisher's Note Springer Nature remains neutral with regard to jurisdictional claims in published maps and institutional affiliations.

Springer Nature or its licensor (e.g. a society or other partner) holds exclusive rights to this article under a publishing agreement with the author(s) or other rightsholder(s); author self-archiving of the accepted manuscript version of this article is solely governed by the terms of such publishing agreement and applicable law.